Charge Transport versus Recombination in Dye-Sensitized Solar Cells Employing Nanocrystalline TiO_2 and SnO_2 Films

Alex N. M. Green,[†] Emilio Palomares,[†,‡] Saif A. Haque,[†] Jan M. Kroon,[§] and James R. Durrant*[,†]

Center for Electronic Materials and Devices, Department of Chemistry, Imperial College of Science, Technology, and Medicine, Exhibition Road, London SW7 2AZ, United Kingdom, Institut de Ciencia Molecular, Universitat de Valencia, 46100 Burjassot, Valencia, Spain, and Department Solar Energy, Energy Research Centre of The Netherlands, P.O. Box 1, 1755 ZG Petten, The Netherlands

Received: January 10, 2005; In Final Form: April 26, 2005

We report a comparison of charge transport and recombination dynamics in dye-sensitized solar cells (DSSCs) employing nanocrystalline TiO_2 and SnO_2 films and address the impact of these dynamics upon photovoltaic device efficiency. Transient photovoltage studies of electron transport in the metal oxide film are correlated with transient absorption studies of electron recombination with both oxidized sensitizer dyes and the redox couple. For all three processes, the dynamics are observed to be 2−3 orders of magnitude faster for the SnO_2 electrode. The origins of these faster dynamics are addressed by studies correlating the electron recombination dynamics to dye cations with chronoamperometric studies of film electron density. These studies indicate that the faster recombination dynamics for the SnO_2 electrodes result both from a 100-fold higher electron diffusion constant at matched electron densities, consistent with a lower trap density for this metal oxide relative to TiO_2, and from a 300 mV positive shift of the SnO_2 conduction band/trap states density of states relative to TiO_2. The faster recombination to the redox couple results in an increased dark current for DSSCs employing SnO_2 films, limiting the device open-circuit voltage. The faster recombination dynamics to the dye cation result in a significant reduction in the efficiency of regeneration of the dye ground state by the redox couple, as confirmed by transient absorption studies of this reaction, and in a loss of device short-circuit current and fill factor. The importance of this loss pathway was confirmed by nonideal diode equation analyses of device current−voltage data. The addition of MgO blocking layers is shown to be effective at reducing recombination losses to the redox electrolyte but is found to be unable to retard recombination dynamics to the dye cation sufficiently to allow efficient dye regeneration without resulting in concomitant losses of electron injection efficiency. We conclude that such a large acceleration of electron dynamics within the metal oxide films of DSSCs may in general be detrimental to device efficiency due to the limited rate of dye regeneration by the redox couple and discuss the implications of this conclusion for strategies to optimize device performance.

Introduction

Nanocrystalline metal oxide films are attracting interest for applications including photocatalysis,[1] electrochromic devices,[2] and photovoltaic energy conversion.[3] For such applications, both the semiconducting charge-transport properties of the film and the interfacial electron-transfer dynamics occurring at the surfaces of the constituent metal oxide nanoparticles are critical to device function. In this paper, we report a detailed comparison of these charge-transport and interfacial electron-transfer dynamics for two different metal oxides, TiO_2 and SnO_2, and thereby consider the relative suitability of these metal oxides for use in dye-sensitized photoelectrochemical solar cells.

Dye-sensitized solar cells (DSSCs) are based upon the sensitization of mesoporous, nanocrystalline metal oxide films to visible light by the adsorption of molecular dyes. Photoinduced electron injection from the sensitizer dye into the metal oxide conduction band initiates charge separation. Subsequently, the injected electrons are transported through the metal oxide film to one device electrode, while a redox-active electrolyte is employed to rereduce the dye cation and transport the resulting positive charge to a platinum counter electrode. Efficiencies of DSSCs of up to 10.4%[4] have been reported for devices employing nanocrystalline TiO_2 films. Several studies have addressed the use of alternative metal oxides including SnO_2,[5,6] ZnO,[7,8] and Nb_2O_5.[9,10] SnO_2 has in particular attracted attention as an attractive alternative to TiO_2 in DSSCs due to its higher electronic conductivity and electron mobility when compared to TiO_2.[11] Such faster electron transport dynamics should in principle favor efficient collection of injected electrons at the device electrode, thereby minimizing interfacial charge recombination losses to either dye cations or oxidized redox species in the electrolyte and improving device performance. However, despite this, to date only rather poor device efficiencies have been reported for DSSCs employing nanocrystalline SnO_2.

Investigations into the factors limiting the performance of SnO_2-based DSSCs have been limited to date. The conduction band potential has been reported to be 0.4 V more positive than that of nanocrystalline TiO_2.[3,12−14] This has been suggested to

* Author to whom correspondence should be addressed. Fax: 44 (0)20 7594 5801. E-mail: j.durrant@imperial.ac.uk.
[†] Imperial College of Science, Technology, and Medicine.
[‡] Universitat de Valencia.
[§] Energy Research Centre of The Netherlands.

10.1021/jp050145y CCC: $30.25
Published on Web 06/02/2005

lead to a lower attainable open-circuit voltage (V_{oc}) for SnO_2 devices, favoring charge recombination losses of injected electrons with the redox electrolyte.[15] Several approaches have been employed to improve the efficiency of SnO_2-based DSSCs, including increasing particle size[16] and substitution of the commonly used Ru dyes with several alternatives.[17,18] Significant improvements in the performance of SnO_2-based DSSCs have been achieved by the use of an insulating barrier coating on the surfaces of the SnO_2 nanoparticles, but even with the use of such barrier layers, device efficiencies remain lower than those reported for equivalent TiO_2-based devices.[5,6]

The primary aims of this paper are to elucidate the factor(s) resulting in relatively poor device performance in SnO_2-based DSSCs and thereby to address the potential for SnO_2 as a replacement for TiO_2 in such devices. A key element of this study is consideration of whether faster electron transport dynamics are indeed beneficial to device function. One of the factors complicating optimization of DSSC efficiency is the close correlation between the different processes determining device efficiency.[19] In particular, it has been widely reported that the relatively slow electron transport dynamics in TiO_2-based DSSCs result from electron trapping in sub-band-gap states of the metal oxide.[20,21] However, such electron trapping has also been reported to be key in retarding interfacial charge recombination dynamics in such devices.[20,22] The close correlation between electron transport and interfacial recombination dynamics has recently been emphasized in a study of lithium intercalation into nanocrystalline TiO_2 films.[22] Whether the net effect of such electron trapping is beneficial or detrimental to device function is at present an unresolved question and is a key issue addressed in this paper.

In the study reported here, we employ SnO_2 and TiO_2 films selected to be as structurally similar as possible and employ dye-sensitizing conditions to achieve matched dye loading on each film. As expected, we find relatively low device efficiency for SnO_2 devices. We employ transient photovoltage measurements to confirm the presence of faster electron transport dynamics in the SnO_2-based device. We then extend our studies to transient optical spectroscopy of interfacial recombination dynamics to both oxidized sensitizer dyes and oxidized redox couples. The origin of the faster recombination dynamics observed for the SnO_2 is addressed by studies as a function of electrochemical bias applied to the film and correlated with electrochemical studies of film electron densities. We then turn to consideration of charge separation dynamics, in particular the kinetic competition between the electron recombination to the dye cation and the desired rereduction of the dye cation by the redox electrolyte, and demonstrate that this is a key factor limiting performance of SnO_2-based DSSCs. We finally address the potential for optimization of device function, in particular the use of metal oxide barrier layers to minimize interfacial recombination losses.

Materials and Methods

Film Fabrication. The colloids have been prepared following procedures reported earlier.[23−25] Approximately 388 g of titanium tetraisopropoxide was rapidly added to 820 mL of distilled water and stirred for 1 h. A white precipitate was formed instantaneously by hydrolysis of the titanium isopropoxide, which was filtered using a glass filter and washed three times with small portions of distilled water. The filter cake was then transferred into a titanium autoclave and mixed with 60 g of 25% tetramethylammonium hydroxide (TMAH) solution. Peptization occurred during heating the mixture in the autoclave at 130 °C for approximately 12 h. To realize particle growth up to the desired size of approximately 20 nm, the resulting suspension was heated for 12 h in an autoclave at a temperature of 180 °C. The colloidal particles were transferred from the aqueous suspension into a mixture of terpineol and ethylcellulose to prepare a screen-printable paste. The 4-μm-thick films were deposited by "doctor blading" on TEC-15 F/SnO_2 conducting glass microscope slides between single strips of Scotch Magic Tape (thickness of 60 μm) placed along the slide edges. The films were left to dry in air until they were transparent, then sintered at 450 °C for 30 min. [26]

SnO_2 paste was prepared following the route published by Chappel et al.[16] utilizing an aqueous colloidal suspension (15% w/v) of SnO_2 nanoparticles (Alfa Aesar, particle diameter 15 nm). The paste was formed by first adding 1 g of acetic acid to 37 g of SnO_2 colloidal solution. The resulting mixture was covered and allowed to stir for 36 h. The solution was autoclaved at 240 °C for 80 h, then allowed to cool. The colloids were redispersed by a 60 s full-power burst from a Branson Ultrasonics sonic horn, and then 3 g of Carbowax 20000 was added. The resulting paste was comprised of 14% (w/v) 18−20 nm diameter SnO_2 particles and was stirred overnight to ensure homogeneity throughout. The 4-μm-thick films were then produced by "doctor blading" (as detailed above) and sintered at 450 °C for 30 min.

The MgO coating solution was prepared from magnesium isopropoxide (Aldrich) dissolved in ethanol (0.15 M). The solutions were prepared under anaerobic conditions in a glovebox, but once prepared, the coating of the nanocrystalline metal oxide films was carried out on the lab bench under ambient conditions. Nanocrystalline SnO_2 films were exposed to water vapor for 1 min and then dried at 120 °C. The films were then immersed in the coating solutions for 20 min at 70 °C. The films were then removed and sintered at 450 °C for a further 20 min. In comparisons of coated and uncoated films, uncoated control films were subjected to the same temperature variations as the coated films.

Cell Fabrication. Nanocrystalline metal-oxide-coated conducting glass slides were cut into pieces of 2.5 cm × 1.5 cm, and the excess metal oxide was scraped off to give an active area of 1 cm^2. Sensitization of the photoelectrodes with the ditetrabutylammonium salt of $RuL_2(NCS)_2$ (where L is 4,4′-dicarboxy-2,2′-bipyridyl) was achieved by immersing the electrodes in a 1 mM solution of dye in 1:1 acetonitrile/*tert*-butyl alcohol for up to 4 h until the dye loading was the same, followed by rinsing in ethanol to remove unadsorbed dye. For counter electrode fabrication, uncoated conducting glass slides were also cut into pieces of 2.5 cm × 1.5 cm, and 1 mm^2 holes were drilled through the glass (using an electric drill) at the corners of a 1 cm × 1 cm square centered on the glass. A thin film of H_2PtCl_6 (0.01 M in ethanol) was then spread over the conducting glass electrode, which was allowed to dry in air prior to firing at 400 °C for 20 min. The TiO_2 and platinum counter electrode was then sealed together with a transparent film of Surlyn 1472 (Dupont) cut as a frame around the nanocrystalline TiO_2 film. An acetonitrile-based electrolyte containing 0.05 M iodine, 0.1 M lithium iodide, 0.5 M 4-*tert*-butylpyridine (TBP), and 0.7 M tetrabutylammonium iodide (TBAI) was introduced through the holes drilled in the counter electrode, which were sealed immediately with inert glue (Araldite).

Current−Voltage Device Characterization. Current−voltage measurements were obtained using with a ScienceTech solar simulator and AM 1.5 spectral filter. Calibration of the light intensity was achieved by using band-pass filters of known

transmission combined with a silicon photodiode with independently certified spectral response, calibrated at the ISE Fraunhofer Insitut in Freiburg, Germany. The lamp intensity was adjusted to give close (±5%) agreement with theoretical one sun AM 1.5 intensity over the spectral region of the dye optical absorption (450−700 nm). We note that as the focus of this paper is not to optimize device efficiency, but rather a functional comparison of the two metal oxides, device efficiencies reported here are lower than literature values due to our use of thin metal oxide layers, nonscattering devices, and matched dye-loaded film optical densities.

Chronoamperometry. Chronoamperometric studies of unsensitized metal oxide films were conducted as reported previously[26] in a three-electrode spectroelectrochemical cell employing a MeCN-based redox-inactive electrolyte containing 0.1 M tetrabutylammonium perchlorate and 0.1 M lithium perchlorate. To minimize water content of the electrolyte, all preparations was carried out under a nitrogen atmosphere in a glovebox. The water content of the resulting electrolyte was determined using a Metrohm 737 Coulometer. All electrolytes used had values of 200−600 ppm H_2O. Prior to all chronoamperometric measurements, the nanocrystalline TiO_2 or SnO_2 electrode was heated to 450 °C for 10 min to remove adsorbed moisture and organics. This electrode was then held in a platinum clip and used as a working electrode in a photoelectrochemical cell. The counter electrode was fine platinum mesh, and an Ag/AgCl reference electrode was used with an Autolab PGStat 12 potentiostat to provide potential control to the experiment. Argon was bubbled throughout the electrolyte between readings to maintain an anaerobic atmosphere and to ensure proper mixture of the electrolyte throughout the experiment. To reach equilibrium in the cell, the applied voltage was kept constant for 10 min. A bias step of −25 mV was then applied, and the current transient was recorded and integrated as detailed below. This procedure was repeated at 100 mV intervals for both the TiO_2 and SnO_2 nanocrystalline films.

Transient Spectroscopy. Transient absorption data were conducted on both complete DSSCs and on dye-sensitized electrodes as reported previously.[27] Dye-sensitized nanocrystalline SnO_2 and TiO_2 films were placed either into the spectroelectrochemical cell as detailed above or in the "sandwich" configuration complete DSSCs. For collection of transient absorption data, samples were excited at 550 nm employing a PTI GL-3300 nitrogen laser-pumped dye laser (14 $\mu J/cm^2$ 0.8 Hz). The photoinduced change in optical density was monitored using a 100 W tungsten lamp light beam with 20 nm bandwidth monochromators before and after the sample and home-built detection electronics and digitized on a TDS-220 Tektronics DSO. Transient studies of complete DSSCs were conducted under open-circuit conditions with minimal ambient lighting resulting in typical "resting" cell voltages of 0.1 and 0.15 V for the SnO_2 and TiO_2 films, respectively, corresponding to metal oxide Fermi levels relative to Ag/AgCl of approximately −0.2 and −0.15 V, respectively.

Photovoltage Measurements. Photovoltage transients were recorded on working DSSCs prepared as detailed above. Cells were placed in the sample holder in front of the laser light guide in the probe beam, wired directly to a 1 MΩ terminator on the oscilloscope, and excited by a short laser pulse as for the transient absorption experiments detailed above. The photoinduced change in photovoltage was collected from the oscilloscope using home-built data analysis software. Experiments were conducted with optical excitation through the device counter electrode, with the photovoltage rise time corresponding to a transit time for electrons through the metal oxide film. "Dark" initial voltages prior to the optical pulse were as for the transient absorption experiments detailed above. A detailed analysis of this technique and the theoretical modeling thereof will be reported elsewhere.

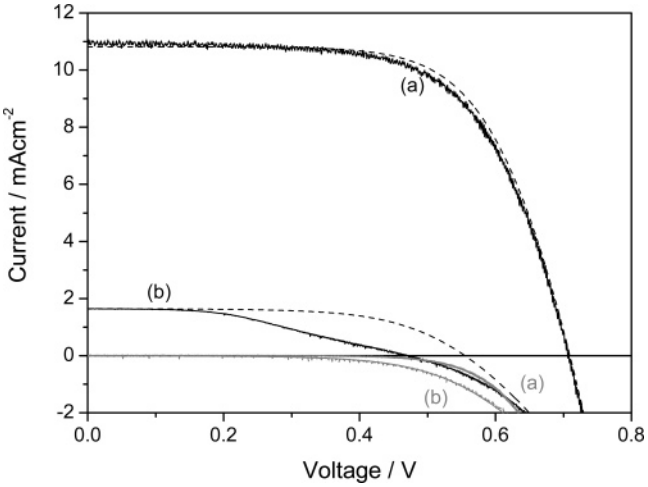

Figure 1. Current−voltage characteristics for DSSCs employing 4-μm-thick, nonscattering (a) TiO_2 and (b) SnO_2 nanocrystalline metal oxide films and matched dye loadings. Data collected under simulated AM 1.5 irradiation (black lines) and in the dark (grey lines). Dashed lines are fits to the data based on the nonideal diode equation (eq 2); see text for details.

Results and Discussion

Materials and Device Characterization. The nanocrystalline, mesoporous SnO_2 and TiO_2 films employed for this study were selected to be as structurally similar as possible. Structural analyses of the SnO_2 films indicated a particle diameter of ∼18 nm, porosity of 55%, and surface area of 60−80 $m^2\ g^{-1}$. For the TiO_2 films, a particle diameter of ∼24 nm was obtained with a porosity of 45% and a surface area of 60−70 $m^2\ g^{-1}$. In both cases, the films produced were of thickness 4 ± 0.5 μm. Dye-sensitization conditions were optimized to ensure matched dye loadings (peak dye optical density at 535 nm of 1.2) for both metal oxides. We can conclude that the differences in photovoltaic performance of DSSCs fabricated from these two metal films will primarily result from differences in the underlying charge-transport and electron-transfer properties of the metal oxides employed.

Photovoltaic device performances of DSSCs fabricated with these metal oxide films are shown in Figure 1. It is apparent that device efficiencies employing the SnO_2-based devices exhibit poor photovoltaic performance relative to the TiO_2 devices, consistent with previous literature studies.[5,6] We note that very significant improvements in device performance can be obtained by coating the nanocrystalline SnO_2 films with insulating barrier layers,[28−32] an issue that we address in detail below. However, we consider first the origin of the low device efficiencies observed for the uncoated SnO_2 films.

Electron-Transport Studies. Previous studies have reported much higher electrical conductivities[11] and electron mobilities[33,34] for SnO_2 relative to TiO_2, with this difference indeed being the primary motivation for previous studies of SnO_2 films in dye-sensitized solar cells.[5,6] Confirmation and quantification of the higher electron-transport dynamics in the SnO_2 films employed relative to the TiO_2 control films were addressed by measuring photovoltage rise transient measurements on complete DSSCs employing the two metal oxide films, as shown in Figure

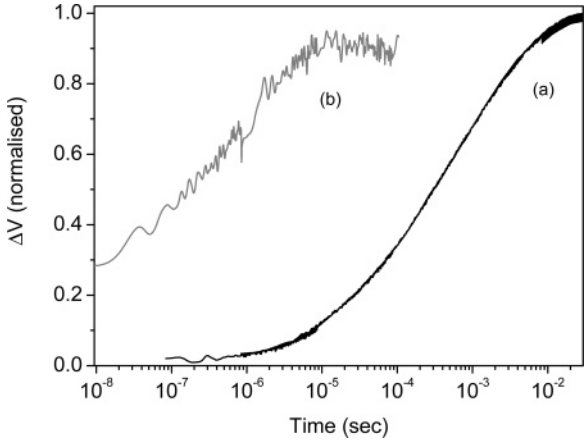

Figure 2. Photovoltage transients for complete DSSCs fabricated with (a) TiO_2 and (b) SnO_2 films following pulsed excitation at 550 nm, employing a redox-active electrolyte of 0.05 M I_2, 0.7 M TBAI, 0.1 M LiI, and 0.5 M TBP. Transients were collected under open-circuit and "dark" ambient conditions ("resting" open-circuit potentials of 0.15 and 0.1 V for a and b, respectively). The peak magnitude of the photovoltage transient was 70 mV for the TiO_2 cell and 9 mV for the SnO_2 cell.

TABLE 1: Comparison of Half-Times for Electron Transport and Recombination Dynamics for the Two Metal Oxides

	electron transport dynamics[a,b]	electron recombination to redox couple[a,c]	electron recombination to the dye cation[d,e]
TiO_2	200 μs	10 ms	800 μs
SnO_2	200 ns	9 μs	4 μs

[a] Determined from studies of complete DSSCs. [b] $t_{50\%}$ determined from photovoltage transients (Figure 2). [c] $t_{50\%}$ determined from transient absorption data with a probe wavelength of 1000 nm (Figure 4). [d] Determined from studies of dye-sensitized films in a redox-inactive electrolyte. [e] $t_{50\%}$ determined from transient absorption data with a probe wavelength of 800 nm (Figure 3).

2. It is apparent that the photovoltage rise transient is approximately 3 orders of magnitude faster for the SnO_2 electrode compared to that of the TiO_2 electrode, consistent with published mobility data for the two metal oxides. The half-times for these transients are tabulated in Table 1.

Interfacial Charge Recombination Dynamics. We turn now to comparison of the interfacial charge recombination dynamics observed for the two metal oxides. Recombination of metal oxide electrons to both the dye cation species and the redox electrolyte are addressed (Figures 3 and 4, respectively). Recombination to the dye cation was monitored in the absence of the redox couple by placing the dye-sensitized films in a three-electrode spectroelectrochemical cell with redox-inactive electrolyte. Pulsed excitation of dye-sensitized nanocrystalline films under these conditions results in a broad absorption increase centered at 800 nm assigned to a ligand-to-metal charge-transfer transition of the dye cation.[35] In the absence of a redox couple to rereduce the dye cation, this species recombines with electrons in the metal oxide film, observed as a decay of the transient signal to zero. Typical decay transients are shown in Figure 3, with applied potentials corresponding to the rest potentials of the complete DSSCs employed in the photovoltage transients details above. It is apparent that the decay of dye cation on the SnO_2 electrode is ~2 orders of magnitude faster than that of the dye cation on the TiO_2 substrate, with the recombination half-times being detailed in Table 1.

The charge recombination dynamics shown for the two metal oxides in Figure 3 both exhibit highly nonexponential, dispersive

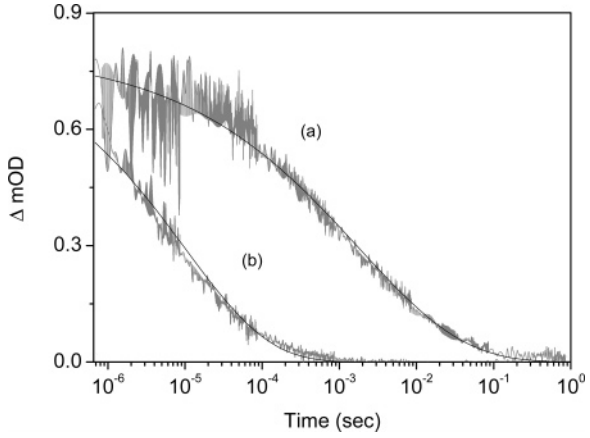

Figure 3. Transient absorption data of dye-sensitized nanocrystalline (a) TiO_2 and (b) SnO_2 films at +100 mV (TiO_2) and +200 mV (SnO_2) applied bias versus a Ag/AgCl reference electrode. Data were collected at a probe wavelength of 800 nm and pump wavelength of 550 nm in a three-electrode photoelectrochemical cell at room temperature. The experiment employed an anhydrous acetonitrile electrolyte containing 0.1 M tetrabutylammonium perchlorate and 0.1 M lithium perchlorate. The smooth lines are exponential fits to the experimental data with the stretch parameter $\alpha \approx 0.3 \pm 0.05$ for both metal oxides.

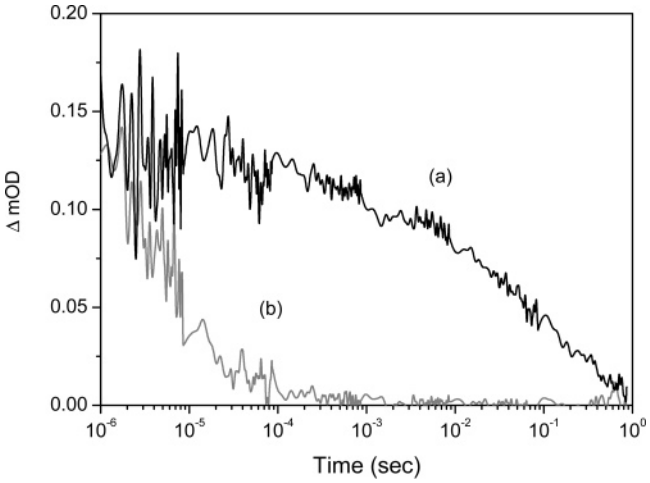

Figure 4. Transient absorption data of a dye-sensitized nanocrystalline (a) TiO_2 and (b) SnO_2 dye cell. Data were collected at a probe wavelength of 1000 nm, corresponding to the absorption of photoinjected electrons in a "sandwich cell" configuration employing a typical redox-active electrolyte of 0.05 M I_2, 0.7 M TBAI, 0.1 M LiI, and 0.5 M TBP. Experimental conditions were carried out under open-circuit conditions in the dark.

dynamics. Numerical fits of these transients to a stretched exponential function ($\Delta OD \propto \exp(-t/\tau)^{\alpha}$) give excellent fits (smooth lines in Figure 3), with values of the stretch parameter $\alpha \approx 0.3 \pm 0.05$ for both metal oxides. This stretched exponential behavior has previously been reported for both TiO_2 and ZnO electrodes[26] and assigned to the recombination dynamics controlled by electron transport through an energetic distribution of trap states within the metal oxide film. The observation of similar stretched exponential behavior for the dye-sensitized SnO_2 films strongly suggests that such electron trapping may also play a key role in determining recombination dynamics for this metal oxide, an issue that we discuss in more detail below.

Figure 4 extends these transient optical studies of charge recombination to charge recombination of injected electrons with the redox electrolyte in complete DSSCs. In these studies, we employ a probe wavelength of 1000 nm. At this wavelength, the transient optical signal is dominated by the absorption of

electrons photoinjected into the metal oxide, with neither the dye cation species nor the redox couple exhibiting significant optical signals at this wavelength This assignment is supported by the complete loss of this signal when employing a ZnO electrode, an electrode for which conduction band electrons are reported only to absorb electrons for wavelengths greater than 1000 nm (data not shown).[26] The resulting transient electron decays for the SnO_2 and TiO_2 dye-sensitized solar cells at an open circuit can be seen in Figure 4. A rapid acceleration in electron decay can clearly be observed for the SnO_2-based device relative to the TiO_2 device, assigned to the accelerated recombination of metal oxide electrons with the redox couple, with the recombination half-times again being detailed in Table 1.

It is clearly apparent from the photovoltage rise and transient absorption decay half-times summarized in Table 1 that there is a correlation between the faster electron transport data for the SnO_2 films and faster recombination dynamics for these films. This correlation between transport and recombination dynamics is consistent with a recent study of the influence of lithium intercalation into nanocrystalline TiO_2 films.[22] It is furthermore consistent with our previous studies[20] that have demonstrated that interfacial recombination dynamics in dye-sensitized TiO_2 films are strongly influenced by electron dynamics within the metal oxide nanoparticles.

Correlating Recombination Dynamics and Film Electron Density. Previous studies have shown that the conduction band edge for SnO_2 is ~0.4 V positive of that for TiO_2. The transport and recombination studies were all undertaken with the metal oxide film potentials corresponding to the "dark" resting state of the complete devices (0.15 and 0.2 V vs Ag/AgCl for TiO_2 and SnO_2 films, respectively). As such, the film Fermi level is expected to be closer to the conduction band edge of the metal oxide for the SnO_2 film. It is therefore possible that the faster dynamics observed for the SnO_2 films may originate from the consequently higher electron density in this film relative to the TiO_2 rather than a difference in the underlying single-electron behavior (electron mobility or electron-transfer rate constant). To address this issue further, we conducted a study of the dynamics of electron recombination to the dye cation as a function of electrical bias applied to the metal oxide electrode in the three-electrode spectroelectrochemical cell and correlated these studies with chronoamperometric measurements of film electron densities determined under the same experimental conditions.

Electron densities were determined from potential step chronoamperometry following procedures detailed previously.[26] Typical transients are shown in Figure 5a, with the electron densities determined from these transients shown in Figure 5b. As reported previously, TiO_2 films exhibited a biphasic chronoamperometric response. The fast phase (milliseconds to seconds), assigned to capacitative charging of the film, was employed to calculate the film electron densities reported here. The slow phase (minutes time scale) is assigned to lithium intercalation processes. After the application of a potential step to dye-sensitized TiO_2 films, the charge recombination dynamics are invariant on the time scale of this slow phase (data not shown); for this reason, this phase is not included in the electron density calculations reported here. For the SnO_2 films, the slow phase was not observed in the chronoamperommetric data for the potential range under consideration here (only being observed at strongly negative potentials), suggesting a significantly larger activation barrier to lithium intercalation processes for this metal oxide.

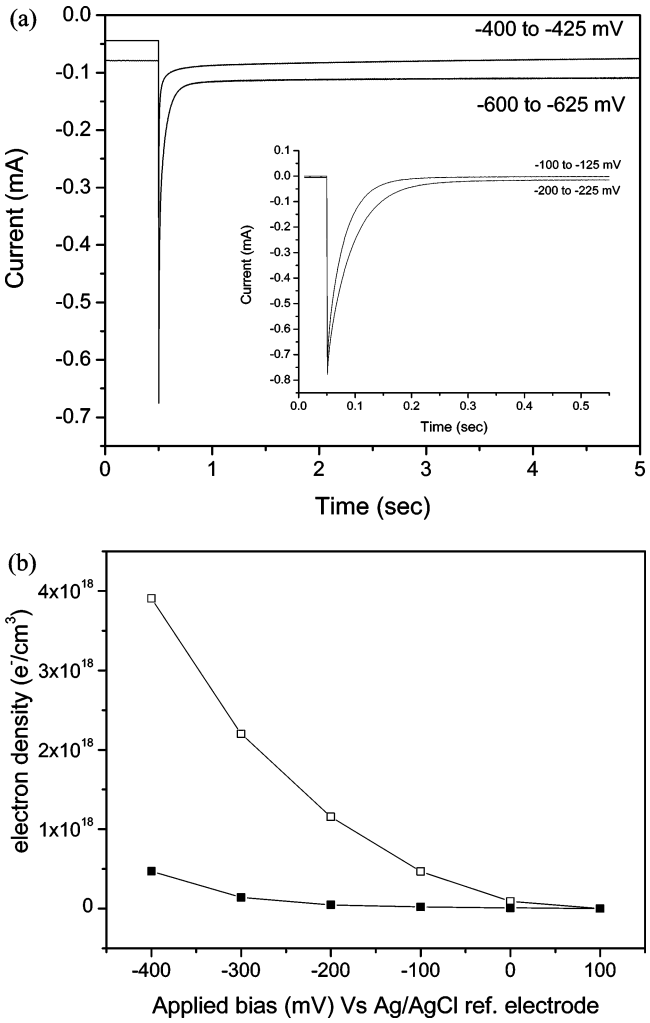

Figure 5. (a) Chronoamperometric transients for a 4 μm TiO_2 film (black) and a 4 μm SnO_2 film (grey). The experimental conditions were as for Figure 3. Prior to each voltage step, the films were equilibrated at the starting potential for 5 min. (b) Plot of the electron density added to the TiO_2 (■) and SnO_2 (□) films over the bias ranges shown. Other experimental conditions were as for Figure 3.

For both metal oxides, it is apparent that the film electron densities increase upon the application of more negative applied potentials. An approximately exponential increase in electron density can be observed for both metal oxide films as a function of applied potential, consistent with our previous studies of TiO_2 and ZnO films (We note the TiO_2 films reported here show lower electron densities at a given potential than those that we have reported previously. This is consistent with the more basic conditions employed in film synthesis, as discussed in detail in ref 24). It is furthermore apparent that the electron density data is shifted by 300 ± 50 mV to more negative potentials for the TiO_2 films relative to those of the SnO_2 films. This shift is consistent with previous reports of a ~0.4 V shift of the SnO_2 conduction band edge relative to TiO_2.[3,12−14]

Transient absorption studies of the charge recombination dynamics of metal oxide electrons to dye cations, as presented in Figure 3, were extended to the range of bias potentials employed in the chronoamperometric studies of electron density. In all cases, nonexponential, dispersive recombination dynamics were observed. Figure 6 shows a plot of the half-time ($t_{50\%}$) for charge recombination against the applied potential for both metal oxides. The data reported for the TiO_2 electrode is similar to that we have reported previously for analogous electrodes, exhibiting a bias-independent region at more positive potentials

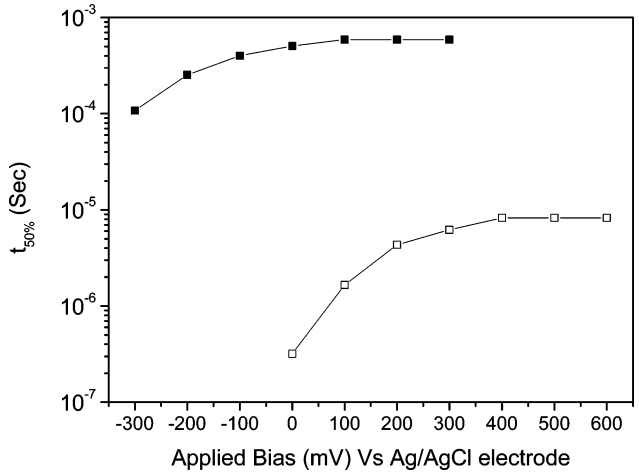

Figure 6. Half-times ($t_{50\%}$) for charge recombination to dye cations determined from the absorption transients shown in Figure 3 plotted as a function of applied bias for dye-sensitized nanocrystalline TiO_2 (■) and SnO_2 (□) films. The charge recombination dynamics were independent of applied voltages greater than +100 and +400 mV for the TiO_2 and SnO_2 films, respectively. Other experimental details were as for Figure 3.

assigned[27] to recombination of dye cations with electrons photoinjected by the laser pulse (~1 electron/nanoparticle) and an acceleration in recombination dynamics toward more negative applied potentials as the density of electrons introduced to the film by the externally applied bias exceeds that injected by each laser pulse. It is apparent from Figure 6 that an analogous bias dependence of the recombination half-time is observed for the SnO_2 electrodes. The recombination half-times are slower for TiO_2 electrodes compared to the SnO_2 electrodes over the whole bias range studied. It is furthermore apparent that the onset of the bias dependence of the recombination half-time is shifted 300 mV ± 50 mV to more positive biases for the SnO_2 film relative to the TiO_2 film. This shift in bias dependence of the recombination half-times for the SnO_2 electrode relative to the TiO_2 shows a clear correlation with the shift in the bias dependence of the electron density determined from the chronoamperometry data given in Figure 5.

We have previously addressed in detail the correlation between the bias dependence of electron density and recombination dynamics for a range of different experimental conditions.[26,27] The bias dependence of electron density is consistent with an exponential tail of localized states extending below the conduction band edge (electron "trap" states). The strong dependence of recombination half-time upon the applied bias has previously been shown to result from progressive filling of this tail of trap states by the applied bias, resulting in both an increase in electron density and an increase in electron mobility as progressively shallower traps are occupied. Consistent with this picture, a close correlation has previously been observed of the bias dependence of electron densities and charge recombination half-times both as a function of electrolyte composition and metal oxide employed. The comparison that we report here is fully consistent with the model and provides further evidence that electron dynamics in the SnO_2 electrode are influenced by electron trapping/detrapping dynamics through a distribution of sub-band-gap localized states.

In addition to the shift in the bias dependence of the recombination half-time between the two metal oxides, it is apparent from Figure 6 that the recombination dynamics for the SnO_2 films are at least 2 orders of magnitude faster than those observed for the TiO_2 over the complete bias range studied. It is of particular importance that the recombination dynamics in the limit of positive applied bias (the bias-independent "plateau" regions) are 2 orders of magnitude faster for the SnO_2 film. In this limit of positive applied potential, the electron densities in the films are dominated by photoinjected electrons (with negligible electron density prior to the optical excitation). Given that the experiments employed identical excitation conditions and matched dye loadings and assuming no difference in electron injection yield for the two metal oxides, consistent with previous studies,[36] it can be concluded that the recombination dynamics observed in this limit correspond to those observed with similar electron densities in the two films. The accelerated recombination dynamics observed for the SnO_2 film compared to the TiO_2 in this positive bias limit therefore cannot derive from any difference in electron density between the two films but rather from a faster underlying rate constant for the charge recombination process.

The origin of the faster charge recombination rate constant for the SnO_2 electrode is unclear. Such recombination dynamics are dependent upon both the interfacial electron-transfer rate constant and on the effective electron diffusion constant within the metal oxide.[37] Considering the interfacial electron transfer first, faster recombination dynamics may derive from stronger electronic coupling between the metal oxide and the adsorbed sensitizer dye for the SnO_2 film. Such an increased coupling would however be inconsistent with a recent comparison of electron injection dynamics for dye-sensitized TiO_2 and SnO_2 electrodes, which were found to be indicative of weaker electronic coupling for SnO_2 compared to TiO_2 electrodes.[36] Rather, the faster recombination rate constant for the SnO_2 would appear to be more consistent with a higher effective electron diffusion constant for the SnO_2 film, in agreement with the transport data reported above. Such a faster effective diffusion constant may result from a lower trap density for SnO_2 relative to that of TiO_2. For an exponential density of states and matched electron densities (as employed for the charge recombination studies in the limit of positive applied bias), such a lower trap density would result in lower activation barriers to thermal detrapping and therefore a faster effective electron diffusion constant.

We conclude that the faster recombination dynamics observed for the SnO_2 films have two origins. First of all, the effective electron diffusion constant at matched electron densities is approximately 2 orders of magnitude greater for the SnO_2 electrode compared to that of the TiO_2 electrode. In addition, the electron density of states is shifted approximately 300 mV to more positive potentials for the SnO_2 film relative to that of the TiO_2 film, resulting in rapid further acceleration of the recombination dynamics at even modest applied potentials. Both factors can be expected to result in enhanced recombination losses for DSSCs employing SnO_2 electrodes, as we address in detail below.

Kinetic Competition between Recombination and Regeneration. The above studies indicate that both electron transport and charge recombination dynamics are 2−3 orders of magnitude faster for SnO_2 electrodes compared to those of TiO_2 electrodes. We turn now to consideration of how these faster dynamics are related to lower photovoltaic device performance and in particular focus on the kinetic competition between charge recombination to the dye cation and the rereduction of the dye cation by the redox electrolyte, which results in regeneration of the dye ground state.

We have shown previously that the regeneration reaction results in the formation of I_2^- species

$$\text{dye}^+ + 2\text{I}^- \rightarrow \text{dye} + \text{I}_2^- \quad (1)$$

In the DSSCs, this regeneration must be fast relative to charge recombination of the dye cation with metal oxide electrons for efficient device function. The decay dynamics of the dye cation species and the yield of the I_2^- species generated by the regeneration reaction can be monitored in complete DSSCs by transient absorption studies using a probe wavelength of 800 nm.[38] Figure 7 shows such transient absorption data for TiO_2- and SnO_2-based DSSCs (traces a and b, respectively) under open-circuit conditions. For both devices, a biphasic decay transient is observed. Following from the assignments made by Montanari et al.,[38] the fast phase (1−100 μs) is assigned to a loss of dye cation adsorption due to the regeneration reaction, eq 1 above. The slow phase (0.1−1 s) at this probe wavelength is assigned primarily to absorption of I_2^- species generated by this reaction, with decay of this signal resulting primarily from I_2^- dismutation. In the case of TiO_2, the dye cation signal decays with a $t_{50\%}$ of ∼4 μs, several orders of magnitude faster than that observed in Figure 3, where the loss of dye cation signal in the absence of the redox couple is assigned to the recombination of dye cations with photoinjected electrons. This observation is consistent with previously reported rapid regeneration of the dye cation ground state with I^- [38] and leads to the efficient production of the long-lived I_2^- radical species.

In contrast to the TiO_2, the decay dynamics of the dye cation in the complete SnO_2-based DSSCs (Figure 7, trace b) are on a similar time scale to those observed in the absence of a redox couple (Figure 3, trace b), with decay half-times of ∼1 and 8 μs, respectively. It can be concluded that in SnO_2-based devices dye rereduction by the redox electrolyte competes less efficiently with charge recombination to the dye cation. This conclusion is further confirmed by the relatively low amplitude slow phase observed for the SnO_2 in Figure 7, indicating a 3−4-fold reduction in the yield of I_2^- product states of the regeneration reaction. We note that this lower regeneration yield primarily results from the faster recombination dynamics observed for the SnO_2 electrode rather than any difference in the kinetics of the regeneration reaction between the two metal oxides.

Further support for poor dye regeneration limiting the efficiency of SnO_2-based devices comes from simulation of device *J*/*V* data using the nonlinear diode equation[39]

$$I = I_L - I_0(e^{qV_j/mk_BT} - 1) \quad (2)$$

where I_L is the light-intensity-dependent short-circuit current, k_B is Boltzmann's constant, T is temperature, and I_0 and m are fitting constants. The bias drop across the internal junction, V_j, can be related to the externally applied bias, V, through

$$V_j = V + IR_S \quad (3)$$

where R_S is the series resistance of the system. I_0, m, and R_s are assumed to be light-intensity-independent. This diode equation assumes that recombination losses arise solely from the dark current reaction, recombination of TiO_2 electrons with the redox electrolyte, with the photocurrent generation term I_L being independent of voltage. As recombination to the dye cation is strongly voltage-dependent (Figure 6), any significant losses due to this recombination pathway will result in the experimental data not fitting this simple model. Parameters for the dark current losses (I_0, m, and R_S) were determined from fits to the experimental dark *J*/*V* data; the light *J*/*V* data were then fitted by variation of I_L alone. Such fits are shown as dashed lines in Figure 1. It is apparent that an excellent fit is obtained for the TiO_2-based devices, indicating that photocurrent generation can indeed be simulated as the voltage-independent term I_L and therefore that photocurrent generation losses due to recombination to dye cations are negligible for these devices. However, for the SnO_2-based devices, only a poor fit to the light *J*/*V* data is obtained, indicating additional charge recombination losses photocurrent as the device approaches V_{OC} over and above those expected from the dark current data, consistent with significant photocurrent generation losses due to electron recombination to dye cations.

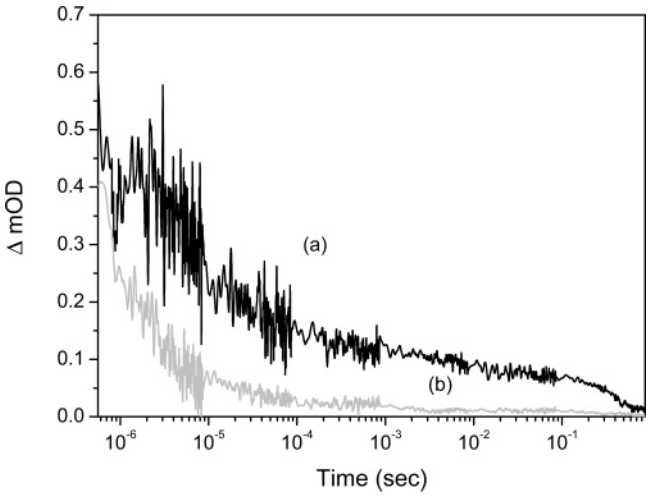

Figure 7. Transient absorption kinetics observed for complete (a) TiO_2 and (b) SnO_2 DSSCs at a probe wavelength of 800 nm. Data were collected in a "sandwich cell" configuration employing a typical redox-active electrolyte of 0.05 M I_2, 0.7 M TBAI, 0.1 M LiI, and 0.5 M TBP under open-circuit and "dark" ambient conditions. The data exhibit biphasic decays. The fast phase (microseconds) is assigned to dye cation decay due to charge recombination with photoinjected electrons and/or rereduction by I^-. The slow phase (milliseconds) is assigned to the decay of I_2^- radicals produced by the rereduction reaction.

Device Optimization: Use of Conformal Barrier Layers. The results reported above indicate there are two factors limiting the performance of SnO_2-based DSSCs compared to TiO_2-based devices. First, the SnO_2 electrode exhibits faster recombination dynamics to the oxidized redox couple. As these faster recombination dynamics are also correlated with faster transport dynamics, this faster recombination most probably does not result in a significant loss in charge collection efficiency at a short circuit, therefore resulting in a lower short-circuit current. These faster recombination dynamics do however result in an enhanced dark current for the SnO_2 devices and consequently limit the device open-circuit voltage and fill factor. Second, the SnO_2 electrode exhibits faster recombination dynamics to dye cations, resulting in the dye regeneration reaction no longer competing efficiently with this reaction. This loss mechanism appears to be significant even for electrode potentials approaching short circuit and can therefore be expected to reduce not only the open-circuit voltage but also the device short-circuit current and fill factor, consistent with the experimental current/voltage data.

Given the above considerations, a key strategy for optimization of the performance of SnO_2-based DSSCs is the minimization of interfacial charge recombination losses. To address this issue, several groups have investigated the use of a metal oxide barrier layer over the SnO_2.[28−32] Our studies to address this issue have employed the barrier-coating strategy that we have reported recently for conformal coatings of nanocrystalline TiO_2 films.[40] A range of metal oxide barrier layers were fabricated, including

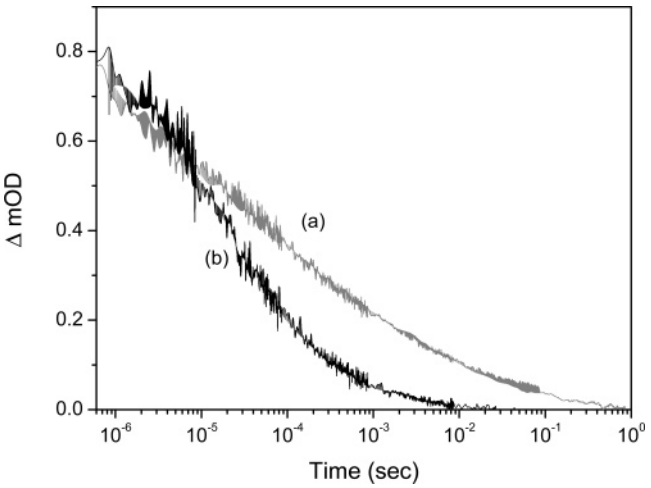

Figure 8. Transient absorption data of dye-sensitized nanocrystalline SnO_2 films (a) with and (b) without an MgO overlayer. The data were collected at a probe wavelength of 800 nm and a pump wavelength of 550 nm, following the decay and absorption of the $RuL_2(NCS)_2$ dye cation for films with matched optical densities covered in ethylene carbonate/propylene carbonate (1:1).

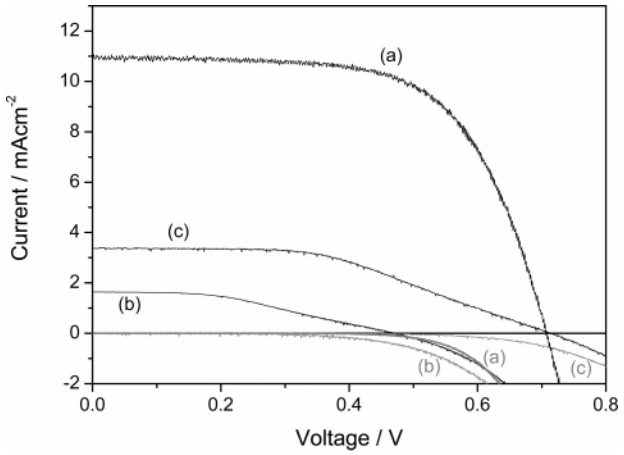

Figure 9. *J*−*V* characteristics of DSSCs employing (a) TiO_2, (b) SnO_2, and (c) SnO_2(MgO) films. Data collected in the dark (grey lines) and under simulated AM 1.5 illumination (black lines). The other experimental conditions were as for Figure 1.

CeO_2 and MgO. For this range of metal oxides, an optimum device performance was found to be obtained by employing a MgO barrier layer, consistent with previous studies.[30]

The blocking function of the MgO barrier layer on the interfacial charge recombination kinetics was determined by monitoring the decay of the photoinduced absorption of the dye cation species in the absence of a redox electrolyte. Figure 8 illustrates the decay kinetics for a dye-sensitized nanocrystalline SnO_2 film in the presence and absence of the MgO overcoat. It is apparent that the presence of magnesium oxide results in a ~4-fold retardation (half-times for the dye cation decay of 8 and 2 μs for the coated and uncoated films, respectively), consistent with the blocking layer function of the MgO overlayer. Moreover, the initial amplitudes of the dye cation transient absorption signal observed for both the coated and the uncoated films were of similar magnitudes (mΔODs of 0.8 at 800 nm), indicating that this barrier layer did not significantly reduce the yield of electron injection from the dye excited state into the SnO_2 conduction band.

Current/voltage characteristics for the SnO_2 solar cells without and with the MgO barrier layer are shown in Figure 9. It is apparent that the MgO barrier layer results in significant improvement in all device characteristics and an overall improvement in device efficiency from 0.5% to 1.2%. Indeed, this barrier layer is sufficiently effective at blocking interfacial charge recombination such that the dark current for the MgO/SnO_2 device is in fact lower than that of the TiO_2 device, resulting in a good device open-circuit voltage. Nevertheless, the short-circuit current and fill factor of the MgO/SnO_2-based DSSCs remain low relative to the TiO_2-based device, consistent with continued significant losses due to charge recombination to the dye cation competing with the regeneration reaction, and the device efficiency remains low relative to the TiO_2-based control cell.

TABLE 2: Current−Voltage Characteristics for Complete DSSCs Employing 4-μm-Thick Nonscattering Nanocrystalline Metal Oxide Films[a]

	open-circuit voltage V_{oc}/mV	short-circuit photocurrent J_{sc}/mA cm^{-2}	fill factor (FF)	efficiency (η)
TiO_2	710	11.0	66%	5.1%
SnO_2	470	1.7	40%	0.5%
SnO_2 (MgO)	710	3.3	48%	1.2%

[a] Data obtained under simulated AM1.5 illumination.

The potential of metal oxide barrier layers to reduce interfacial charge recombination losses is limited by the need to maintain the efficiency of electron injection. Our studies of metal-oxide-coated TiO_2 films have indicated that increasing the barrier layer thickness can result in further retardation of recombination losses but only at the expense of a reduced charge separation yield. Given the 2−3 orders of magnitude acceleration of interfacial charge recombination dynamics for SnO_2 electrodes relative to TiO_2, it is apparent that relatively thick barrier layers may be necessary for SnO_2 electrodes to reduce interfacial charge recombination to the dye cation to such an extent that it no longer reduces the yield of the dye regeneration reaction. Our own attempts at fabricating such thick barrier layers to optimize device performance suggest that such thick layers are not compatible with achieving a high charge separation yield, with all such devices yielding poorer photovoltaic device efficiencies than the TiO_2 control. We have thus concluded that by the use of such barrier layers alone it is likely to be very difficult to achieve SnO_2 device efficiencies superior to those of TiO_2 controls.

Concluding Remarks

One of the most striking features of TiO_2-based DSSCs is the slow carrier collection dynamics. Extensive frequency and time domain studies of DSSCs have indicated electron transport times through the nanocrystalline TiO_2 film of such devices on the order of 1 ms,[41] consistent with the photovoltage rise transient reported here and many orders of magnitude slower than transport dynamics in alternative silicon-based or organic thin film photovoltaic devices.[42] Such slow transport dynamics are motivating studies to accelerate transport dynamics in DSSCs, including the use of high aspect ratio metal oxide nanorods and the use of alternative metal oxides such as SnO_2, as addressed here. A significant concern in such attempts at device optimization is the possibility that the charge-transport and recombination dynamics may be correlated, with changes to material composition or structure accelerating charge transport and charge recombination in parallel. We have demonstrated here that this correlation is indeed a concern for replacement of TiO_2 electrodes in DSSCs with structurally analogous SnO_2 electrodes. We have furthermore demonstrated that the accelera-

tion of both electron transport and recombination dynamics observed for SnO_2 electrodes directly results in lower device performance, as the faster recombination dynamics results in dye cation rereduction by the redox couple no longer competing successfully with electron recombination to the dye cation.

It can be concluded from our studies reported here that changes to the composition of DSSCs that accelerate both the electron transport and charge recombination dynamics may result in poorer photovoltaic device performance. In this sense, the slow electron dynamics observed for the nanocrystalline TiO_2 are indeed beneficial for efficient device function. It can be concluded that, in this regard, the presence of sub-band-gap trap states in nanocrystalline TiO_2 films are indeed desirable for efficient device function and that the passivation or removal of such states from such films may well result in worse device performance. Faster transport dynamics can only be expected to improve device performance if such accelerated dynamics are not correlated with a parallel increase in recombination dynamics.

One attractive route to improve the *relative* dynamics of charge transport and charge recombination in DSSCs is the addition of conformal barrier layers. Such barrier layers result in slower recombination dynamics without necessarily modulating transport. We note however that the extent to which recombination dynamics are accelerated in SnO_2 films compared to TiO_2 suggest that while this approach is clearly able to improve significantly the performance of SnO_2-based DSSCs it is unlikely to result in a device performance greater than that of equivalent TiO_2-based devices. We further note that an alternative strategy to enhance the relative dynamics of charge transport versus charge recombination may be the specific passivation of surface rather than bulk sub-band-gap states of metal oxide films, although this approach is beyond the scope of the study reported here.

The poor performance of SnO_2-based DSSCs is attributed here, at least in part, to the dye regeneration no longer competing with charge recombination to the dye cation. As such, this argument is dependent upon the kinetics of the regeneration reaction. In alternative DSSCs with faster regeneration dynamics, such as those observed when employing molecular hole conductors,[43] this limitation may not be so critical. SnO_2 may therefore be an attractive alternative to TiO_2 for the development of such solid-state dye-sensitized solar cells but appears to have most probably only limited potential for the optimization of DSSCs employing the I^-/I_2 redox electrolyte.

Acknowledgment. The authors thank the EPSRC and the European Union (Contract No. ENK6-CT-2001-00560 Nanomax) for financial support. E.P. acknowledges the financial support from the European Union (Marie Curie European Fellowship Contract No. HPMF-CT-2002-0144). Supply of the $RuL_2(NCS)_2$ sensitizer dye from Johnson Matthey Ltd. is gratefully acknowledged. We thank Richard Monkhouse (Costronics Ltd.) for excellent technical support, Herman J. P. Smit (ECN) for TiO_2 paste preparation, and Jenny Nelson for helpful discussions.

References and Notes

(1) Li, X.; Green, A. N.; Mills, A.; Durrant, J. R. *J. Photochem. Photobiol., A* **2004**, *162*, 253.

(2) Campus, F.; Bonhote, P.; Gratzel, M.; Heinen, S.; Walder, L. *Sol. Energy Mater. Sol. Cells* **1999**, *56*, 281.

(3) Gratzel, M. *Nature* **2001**, *414*, 338.

(4) Nazeeruddin, M. K.; Pechy, P.; Renouard, T.; Zakeeruddin, S. M.; Humphrey-Baker, R.; Comte, P.; Liska, P.; Cevey, L.; Costa, E.; Shklover, V.; Spiccia, L.; Deacon, G. B.; Bignozzi, C. A.; Gratzel, M. *J. Am. Chem. Soc.* **2001**, *123*, 1613.

(5) Kamat, P. V.; Bedja, I.; Hotchandani, S.; Patterson, L. K. *J. Phys. Chem.* **1996**, *100*, 4900.

(6) Ferrere, S.; Zaban, A.; Gregg, B. A. *J. Phys. Chem. B* **1997**, *101*, 4490

(7) Hoyer, P.; Weller, H. *J. Phys. Chem.* **1995**, *99*, 14096.

(8) Rensmo, H.; Keis, K.; Lindstrom, H.; Sodergren, S.; Solbrand, A.; Hagfeldt, A.; Lindquist, S. E. *J. Phys. Chem. B* **1997**, *101*, 2598.

(9) Sayama, K.; Sugihara, H.; Arakawa, H. *Chem. Mater.* **1998**, *10*, 3825.

(10) Lenzmann, F.; Kruegar, J.; Burnside, S.; Brooks, K.; Gratzel, M.; Ruhle, S.; Cahan, D. *J. Phys. Chem. B* **2001**, *105*, 6347.

(11) Jarzebski, Z.; Marton, P. *J. Electrochem. Soc.* **1976**, *123*, 299C.

(12) Ashbury, J. B.; Hao, E.; Wang, Y.; Ghosh, H. N.; Lian, T. *J. Phys. Chem. B* **2001**, *105*, 4345.

(13) Bauer, C.; Boschloo, G.; Mukhtar, E.; Hagfeldt, A.; *Int. J. Photoenergy* **2002**, *4*, 17.

(14) Tachibana, Y.; Rubtsov, I. V.; Montanari, I.; Yoshihara, K.; Klug, D. R.; Durrant, J. R. *J. Photochem. Photobiol., A* **2001**, *142*, 215.

(15) Tachibana, Y.; Hara, K.; Takano, S.; Sayama, K.; Arakawa, H. *Chem. Phys. Lett.* **2002**, *364*, 297.

(16) Chappel, S.; Zaban, A. *Sol. Energy Mater. Sol. Cells* **2002**, *71*, 141.

(17) Tian, H.; Liu, P.; Meng, F.; Gao, E.; Cai, S. *Synth. Met.* **2001**, *121*, 1557.

(18) Tai, W.; Inoue, K. *Mater. Lett.* **2003**, *57*, 1508.

(19) Haque S. A., Palomares, E., Cho B. M. Green, A. N. M., Hirata, H., Klug, D. R., Durrant J. R. *J. Am. Chem. Soc.* **2005**, *110*, 3456.

(20) Nelson, J.; Haque, S. A.; Klug, D. R.; Durrant, J. R. *Phys. Rev. B* **2001**, *63*, 205321.

(21) Schwarzburg, K.; Willig, F. *J. Phys. Chem. B* **1999**, *103*, 5743.

(22) Kopidakis, N.; Benkstein, K. D.; van de Lagemaat, J.; Frank, A. J. *J. Phys. Chem. B* **2003**, *107*, 11307.

(23) Barbe, C. J.; Arendse, F.; Comte, P.; Jirousek, M.; Lenzmann, F.; Shklover, V.; Gratzel, M. *J. Am. Ceram. Soc.* **1997**, *80*, 3157.

(24) Hore, S.; Palomares, E.; Smit, H.; Bakker, N. J.; Comte, P.; Liska, P.; Thampi, K. R.; Kroon, J. M.; Hinsch, A.; Durrant J. R. *J. Mater. Chem.* **2005**, *15*, 412.

(25) Spath, M.; Sommeling, P. M.; van Roosmalen, J. A. M.; Smit, H. J. P.; van der Burg, N. P. G.; Mahieu, D. R.; Bakker, N. J.; Kroon, J. M. *Prog. Photovoltaics* **2003**, *11*, 207.

(26) Willis, R. L.; Olson, C.; O′Regan, B.; Lutz, T.; Nelson, J.; Durrant, J. R. *J. Phys. Chem. B* **2002**, *106*, 7605.

(27) Haque, S. A.; Tachibana, Y.; Willis, R.; Moser, J. E.; Gratzel, M.; Klud, D. R.; Durrant, J. R. *J. Phys. Chem. B* **2000**, *104*, 538.

(28) Chappel, S.; Chen, S.; Zaban, A. *Langmuir* **2002**, *18*, 3336.

(29) Kumara, G. R. R. A.; Tennakone, K.; Perera, V. P. S.; Konno, A.; Kaneko, S.; Okuya, M. *J. Phys. D: Appl. Phys.* **2001**, *34*, 868.

(30) Kay, A.; Gratzel, M. *Chem. Mater.* **2002**, *14*, 2930.

(31) Park, N.; Kang, M. G.; Ryu, K. S.; Kim, K. M.; Chang, S. H. *J. Photochem. Photobiol., A* **2004**, *161*, 105.

(32) Tennakone, K.; Bandaranayake, P. K. M.; Jayaweera, P. V. V.; Konno, A.; Kumara, G. R. R. A. *Physica E* **2002**, *14*, 190.

(33) Jousse, D.; Constantino, C.; Chambouleyron, I. *J. Appl. Phys.* **1983**, *54*, 431.

(34) Shanthi, E.; Dutta, V.; Banerjee, A.; Chopra, K. L. *J. Appl. Phys.* **1980**, *51*, 6243.

(35) Nazeeruddin, M. K.; Kay, A.; Rodicio, I.; Humphrey-Baker, R.; Muller, E.; Liska, P.; Vlachopoulos, N.; Gratzel, M. *J. Phys. Chem.* **1993**, *97*, 6382.

(36) Stockwell, D.; Ai, X.; Anderson, N.; She, C.; Guo, J.; Lian, T. In *Abstracts of Papers*, 55th Southeast Regional Meeting of the American Chemical Society, Atlanta, GA, Nov 16−19, 2003; American Chemical Society: Washington, DC, 2003; p 777.

(37) Clifford, J. N.; Palomares, E.; Nazeeruddin, Md. K.; Thampi, R.; Graetzel, M.; Durrant, J. R.. *J. Am. Chem. Soc.* **2004**, *126*, 5670−5671.

(38) Montanari, I.; Nelson, J.; Durrant, J. R. *J. Phys. Chem. B* **2002**, *106*, 12203.

(39) Nogueira, A. F.; De Paoli, M. A.; Montanari, I.; Monkhouse, R.; Nelson, J.; Durrant, J. R. *J. Phys. Chem. B* **2001**, *105*, 7517.

(40) Palomares, E.; Clifford, J. N.; Haque, S. A.; Lutz, T.; Durrant, J. R. *J. Am. Chem. Soc.* **2003**, *125*, 475.

(41) Peter, L. M.; Duffy, N. W.; Wang, R. L.; Wijayantha, K. G. U. *J. Electroanal. Chem.* **2002**, *524*, 127.

(42) Tzolov, M.; Finger, F.; Carius, R.; Hapke, P. *J. Appl. Phys.* **1997**, *81*, 7376.

(43) Bach, U.; Tachibana, Y.; Moser, J.; Haque, S. A.; Durrant, J. R.; Graetzel, M.; Klug, D. R. *J. Am. Chem. Soc.* **1999**, *121*, 7445.